HHS Public Access

Author manuscript

Cytometry A. Author manuscript; available in PMC 2020 February 01.

Published in final edited form as:

Cytometry A. 2019 February ; 95(2): 201–213. doi:10.1002/cyto.a.23688.

Improving quality, reproducibility, and usability of FRET-based tension sensors

Evan M. Gates[a], **Andrew S. LaCroix**[a], **Katheryn E. Rothenberg**[a], and **Brenton D. Hoffman**[a]

[a]Department of Biomedical Engineering, Duke University, Durham, NC, 27708, USA

Abstract

Mechanobiology, the study of how mechanical forces affect cellular behavior, is an emerging field of study that has garnered broad and significant interest. Researchers are currently seeking to better understand how mechanical signals are transmitted, detected, and integrated at a sub-cellular level. One tool for addressing these questions is a Förster resonance energy transfer (FRET)-based tension sensor, which enables the measurement of molecular-scale forces across proteins based on changes in emitted light. However, the reliability and reproducibility of measurements made with these sensors has not been thoroughly examined. To address these concerns, we developed numerical methods that improve the accuracy of measurements made using sensitized emission-based imaging. To establish that FRET-based tension sensors are versatile tools that provide consistent measurements, we used these methods, which demonstrate that a vinculin tension sensor is unperturbed by cell fixation, permeabilization, and immunolabeling. This suggests FRET-based tension sensors could be coupled with a variety of immuno-fluorescent labeling techniques. Additionally, as tension sensors are frequently employed in complex biological samples where large experimental repeats may be challenging, we examined how sample size affects the uncertainty of FRET measurements. In total, this work establishes guidelines to improve FRET-based tension sensor measurements, validate novel implementations of these sensors, and ensure that results are precise and reproducible.

Keywords

mechanotransduction; FRET-based biosensor; sensitized emission; FRET efficiency

Introduction:

The effect of mechanical force on cellular behavior is an emerging field of study that has garnered significant interest from diverse disciplines, including cell biology, biophysics, cancer biology, vascular biology, and tissue engineering (1–3). Researchers are often interested in determining which proteins are key to mechanotransduction pathways and how these proteins transmit and/or detect mechanical cues (4–6). Research in this area has

Corresponding Author: Brenton D. Hoffman, Room 1379 CIEMAS, 101 Science Drive, Durham, NC 27710, Phone: 919-660-5154, Fax: 919-684-4488, Brenton.hoffman@duke.edu.

Conflict of Interest:
The authors have no conflict of interest to declare.

predominantly focused on two adhesion structures, namely focal adhesions (FAs) and adherens junctions (AJs), because they serve as linkages between a cell's force-generating actomyosin network and the extracellular environment (4–6). Whereas FAs bind to extracellular matrix proteins, AJs adhere to receptors on adjacent cell membranes (7). Both structures involve hundreds of distinct protein types and exhibit mechanosensitivity, meaning they sense and respond to changes in mechanical loading (4–6).

One tool for studying mechanical load across proteins is a Förster resonance energy transfer (FRET)-based tension sensor, which enables the measurement of molecular-scale forces based on changes in emitted light (4, 8–13). The first calibrated, genetically-encoded FRET-based tension sensor was developed to study vinculin (14), a mechanical linker protein that localizes to both adhesion structures, and solidified the importance of vinculin in mechanosensing and migration (14–19). FRET-based tension sensors have since been readily adopted and engineered into at least 14 different proteins(8), demonstrating the usefulness and importance of this tool.

With the widespread application of tension sensors to diverse proteins and systems, some contradictory data has been observed and the lack of clear standards for the accuracy and reproducibility of these measurements has been noted. In particular, it had been demonstrated that E-cadherin is under constitutive load in Madin-Darby Canine Kidney (MDCK) cells (20) and also exhibits spatial gradients in migrating *Drosophila melanogaster* border cells (21). Another study, however, failed to observe any E-cadherin loading in *D. melanogaster* tissues (22), leading the authors to question the reproducibility of measurements made with tension sensing modules. In this work, we develop a set of approaches for both determining and increasing the limits of FRET-based tension sensor accuracy to address these concerns.

FRET involves the non-radiative transfer of energy from a donor fluorophore in the excited state to a nearby acceptor fluorophore (<10–12 nm separation) in the ground state (23). FRET increases as the distance between the two fluorophores decreases. Typically, FRET is often quantified in one of two ways, using FRET index or FRET efficiency (24, 25). FRET indices have a variety of definitions but are typically semi-quantitative estimates of the sensitized emission of the acceptor fluorophore due to the excitation of donor fluorophore (26). These are relative measurements that are device- and setup-dependent, but generally scale with changes in FRET for single chain sensors containing functional fluorophores (26). For most single chain FRET-based biosensors, such as activity-based or conformational-based biosensors, the absolute distance between fluorophores is of less interest than the relative change of FRET signal within cells or in response to specific treatments (27–29). In these instances, FRET index is often a suitable metric for measuring the relative magnitude and dynamics of interactions within a single cell (30). Alternatively, FRET efficiency is a physical quantification of the fraction of donor excitation events that transfer energy to an acceptor fluorophore (23). This is a device independent, absolute measurement that is directly related to the separation distance of the fluorophores, as well as their orientation and rotational dynamics in some cases (31).

In FRET-based tension sensors, the physical separation of the fluorophores is a key variable. In these sensors, two fluorophores capable of FRET are linked by a deformable element and then inserted between load-bearing domains of a protein to enable the measurement of the forces transmitted across the sensor (10, 32). In the absence of load, the linker has an expected characteristic rest length that depends on the flexibility of the linker (33), and the fluorophore pair is expected to exhibit a corresponding characteristic FRET. When load is applied, the linker stretches, FRET decreases, and the application of load can be determined from the FRET signal. While FRET indices can be used to quantify these relative changes (20, 34), the determination of loads requires the measurement of FRET efficiency (23). The determination of load also requires the sensor to be calibrated, meaning the relationship between the applied load and FRET efficiency has been measured or modeled (14, 33). While there are a variety of instruments for measuring FRET efficiency, they are typically expensive or require advanced equipment as compared to instruments for measuring FRET index (35, 36). In addition, there may be other disadvantages associated with instruments required for measuring FRET efficiency (37). For example, certain techniques, such as fluorescence lifetime imaging microscopy (FLIM) or spectral imaging, involve high-powered lasers and less sensitive detectors, which limit both the spatial and temporal resolution of FRET-based sensors (25, 38, 39).

A suitable, but not often employed, alternative is to determine FRET efficiency using sensitized emission-based imaging (36, 40). Like FRET index measurements, these approaches are fast, sensitive, and can be performed on most standard widefield or confocal microscopes. Compared to FLIM and spectral imaging, this approach is relatively inexpensive, accessible, and has greater spatiotemporal resolution. Due to the high resolution of this approach, spatial gradients in protein loading can be visualized within the cell and sub-cellular structures (33, 41). However, sensitized emission methods require additional calibration steps, including corrections for spectral bleedthroughs and determination of two device- and setting-dependent constants (11, 25, 26, 36). Additionally, it has previously been demonstrated that sophisticated approaches, involving numerical techniques such as maximum likelihood estimation, are required for accurate estimations of FRET efficiency in the limit of low signal to noise (42). As a result, the complexities associated with these steps have often discouraged researchers from pursuing sensitized emission as a method for determining FRET efficiency, despite its advantages over other options.

To reduce challenges and improve the accuracy of FRET-based tension measurements made using sensitized emission, we describe a straightforward and precise numerical technique for estimating the two critical calibration constants. Furthermore, for measurements with relatively high signal to noise ratios (e.g. experiments not performed through photon counting-based methods), we develop an improved numerical approach for the characterization of FRET efficiency on a per-cell basis and validate this method by investigating whether fixation, permeabilization, or immunolabeling perturb function of the tension sensor module. Using the original vinculin tension sensor (VinTS) as an example, we find that these treatments do not affect the function of this sensor, demonstrating that FRET-based tension sensors can be combined with immunofluorescence approaches. Furthermore, we show that our numerical approach enables the detection of small

differences in FRET efficiency between two similar, yet structurally distinct, FRET constructs, clearly demonstrating one as the preferred design. Lastly, we demonstrate guidelines that establish the uncertainty in FRET efficiency measurements associated with a given sample size, enabling *a priori* estimates for experimental design in future work. Together these data establish the usefulness of our numerical approach and affirm FRET-based tension sensors as robust indicators of the mechanical loads experienced by proteins in living cells.

Materials and Methods:

Generation of DNA Constructs

Construction of pcDNA3.1-VinTS, pcDNA3.1-VinTS-I997A, pcDNA3.1-TSMod, pcDNA3.1-VinVenus A206K internal, pcDNA3.1-VinmTFP1 internal, and pcDNA3.1-mTFP1-GGS2-Venus transient expression constructs has been described previously (14, 33, 41, 43). To create additional control constructs to detect the presence of intermolecular FRET, pcDNA3.1-VinTS dark mutants were generated from pcDNA3.1-VinTS, in accordance with previously described methods (44). Specifically, dark mTFP1 and dark Venus A206K were created by mutating either Y71 or Y66, respectively, to leucine. The pertinent primers are listed in Supp. Table 1. To create a low FRET construct useful in calibration approaches (36), pcDNA3.1 mTFP1-TRAF-Venus was constructed using Gibson Assembly. Specifically, the vector backbone containing mTFP1 and Venus A206K fluorescent proteins was derived from pcDNA3.1-TSMod, and the TNFα receptor associated factor (TRAF) domain was isolated from CTV (Addgene #27803) (45). Primers used to assemble pcDNA3.1 mTFP1-TRAF-Venus in a three-fragment Gibson Assembly reaction are detailed in Supp. Table 2. To create plasmids appropriate for lentivirus, pcDNA plasmids were digested with NruI/XbaI and ligated into pRRL vector that had been digested with EcoRV/XbaI.

Cell Culture and Expression of DNA constructs

Mouse embryonic fibroblasts lacking vinculin (vinculin −/− MEFs) were generously provided by Drs. Ben Fabry, Wolfgang Goldman, and Wolfgang Ziegler (46). All MEF lines were maintained in high glucose Dulbecco's Modified Eagle's Medium (D6429; Sigma Aldrich) supplemented with 10% fetal bovine serum (HyClone), non-essential amino acids (Gibco), and antibiotic-antimycotic solution (Sigma Aldrich). HEK293-T cells, used for viral production, were maintained in high glucose Dulbecco's Modified Eagle's Medium with L-glutamine and sodium bicarbonate (D5796; Sigma Aldrich) supplemented with 10% fetal bovine serum (HyClone) and antibiotic-antimycotic solution (Sigma Aldrich). Transient transfection of mammalian expression (pcDNA3.1) constructs was achieved using Lipofectamine 2000 Reagent (Invitrogen) and OptiMEM (Gibco) following the manufacturer's protocol. DNA constructs were introduced to vinculin −/− MEFs using standard lentiviral transduction approaches and cells expressing physiological levels of each vinculin-based sensor were selected as previously reported (41, 43).

To create cell adherent surfaces appropriate for imaging, glass bottom dishes (World Precision Instruments) were incubated with 10 μg/ml fibronectin (Fisher Scientific) in PBS

at 4°C overnight. Dishes were rinsed once with PBS prior to cell seeding. MEFs were seeded with 25,000 cells per dish. For live imaging, cells were spread in culturing media for 2 hours and then switched to imaging media (Medium 199, Gibco) supplemented with 10% fetal bovine serum (HyClone) for another 2 hours. For the fixed condition, cells spread in complete media for 4 hours and were then fixed as described below.

Immunofluorescent Staining

For immunofluorescent labeling, cells were fixed with 4% EM grade, methanol-free paraformaldehyde (Electron Microscopy Sciences, Hatfield, PA) for 10 min and then rinsed with PBS before permeabilization. Cells were treated with 0.1% Triton-X for 5 min and then rinsed with PBS. Fresh, 2% bovine serum albumin (BSA, Sigma Aldrich) in PBS was used as blocking buffer for 30 min. Primary vinculin antibody (Sigma V9131, 1:500 in blocking buffer) was applied for 60 min and then rinsed three times with PBS. Cells were again blocked for 30 min. Secondary antibody (Thermo Fisher, AlexaFluor 647 goat anti-mouse, diluted 1:500 in blocking buffer) was applied for 60 min. Cells were then rinsed three times with PBS. Cells were imaged in PBS.

Imaging

An Olympus inverted fluorescent microscope (Olympus IX83, Tokyo, Japan) was used to image samples. Images were acquired at 60× magnification (UPlanSApo 60X/NA1.35 Objective, Olympus) and illuminated by a LambdaLS equipped with a 300W ozone-free xenon bulb (Sutter Instrument, Novato, CA). The images were captured using a sCMOS ORCA-Flash4.0 V2 camera (Hamamatsu Photonics, Hamamatsu, Japan). The FRET images were acquired using a custom filter set comprised of an mTFP1 excitation filter (ET450/30x; Chroma Technology Corp, Bellows Falls, VT), one of two mTFP1 emission filters (ET485/20nm; Chroma Technology Corp or FF02–485/20–25, Semrock, Rochester, NY), Venus excitation filter (ET514/10x; Chroma Technology Corp), Venus emission filter (FF01–571/72; Semrock) and dichroic mirror (T450/514rpc; Chroma Technology Corp). For sensitized emission FRET microscopy, three images are acquired to calculate FRET efficiency (25). These include imaging the acceptor (Venus excitation, Venus emission), FRET (mTFP1 excitation, Venus emission), and donor (mTFP1 excitation, mTFP1 emission). We note that live and fixed conditions as well as the two mTFP1 emission filters yielded different G and k estimates. For each experimental setup, the appropriate calibration factors were used during the analysis, and equivalent measurements of FRET efficiency were observed. For imaging AlexaFluor 647, we utilized the Cy5 filters from the DA/FI/TR/Cy5–4×4 M-C Brightline Sedat filter set (Semrock) and the associated dichroic mirror (FF410/504/582/669-Di01). Exposure times for imaging of Venus, Teal-Venus FRET, Teal, and Cy5 were 1000ms, 1500ms, 1500ms, and 1000ms, respectively. The motorized filter wheels (Lambda 10–3; Sutter Instrument), automated stage (H117EIX3; Prior Scientific, Rockland, MA), and image acquisition were controlled through MetaMorph Advanced software (Olympus). For live cell imaging, a constant temperature was maintained across the sample using an objective heater (Bioptechs, Butler, PA 150819–13) in conjunction with a stage and lid heater (Bioptechs Stable Z System 403–1926). Live samples were imaged for no more than 1 hour.

Correction of Imaging Artifacts and Determination of Spectral Bleedthroughs

Imaging artifacts were identified and corrected as previously described (11). To measure dark current, approximately 40 images were acquired and averaged in each channel with all shutters closed. To correct for uneven illumination, approximately 10 images were taken for each channel on regions of a dish lacking cells or on a separate cell-free dish. Cell-free dishes were treated the same as the experimental dish and imaged in the same focal plane. Shade images were determined by normalizing by the maximum intensity of each image and averaging across the stack of normalized images. Since cells were plated sparsely, the background intensity of each image was determined by estimating the mode pixel intensity of each image, following corrections for dark current and uneven illumination. To correct for three-dimensional offsets caused by chromatic aberrations and minute hardware misalignments, 500 nm diameter microspheres (Fluoresbrite YG and TetraSpeck) diluted in PBS were incubated on glass-bottom dishes overnight to permit evaporation. After adsorption, dishes were washed three times in PBS and imaged in PBS. After leveling the dish in the stage holder, Z-stacks of 21 images (100nm step size) were acquired. For Fluoresbrite YG beads, donor and FRET channels were imaged. For TetraSpeck beads, acceptor and FRET channels were imaged. Approximately 10 stacks were acquired for each bead type. Custom MATLAB (Mathworks) software was used to perform 3D registration of channels.

To measure spectral bleedthroughs, vinculin −/− MEFs were transfected with either soluble mTFP1 or Venus and imaged in acceptor, FRET, and donor. Prior to estimating bleedthroughs, all images were corrected for anomalies due to dark current, uneven illumination, background intensity, and chromatic aberrations as described above and elsewhere (11). Donor bleedthrough (dbt) is the amount of donor emission captured in the FRET channel, and cross-talk is the amount of donor excited and captured by imaging the acceptor channel. Acceptor bleedthrough (abt) is the amount of acceptor directly excited during FRET imaging, and cross-talk is the amount of acceptor excited and captured by imaging the donor channel. For our system, bleedthroughs do not depend on intensity and cross-talk between the channels is negligible. To determine abt, pixels of similar acceptor intensity were binned for each construct, and the corresponding FRET intensity pixels for each bin was averaged. A linear curve was then fit to the relationship between mean FRET intensity and acceptor intensity. The slope of this fit provided an estimate of abt. The same procedure was used to calculate dbt.

Calculation of FRET Efficiency from Sensitized Emission

FRET was detected through measurement of sensitized emission (36) and calculated using custom written code in MATLAB (47). All analyses were conducted on a pixel-by-pixel basis. Prior to analysis, all images were corrected for dark current, uneven illumination, background intensity, and chromatic aberration as described in the previous section. To correct for spectral bleedthrough in experimental data, pixel-by-pixel FRET corrections were performed according to the equation:

$$F_c = I_f - dbt * I_{dd} - abt * I_{aa} \quad (1)$$

where F_c is the corrected FRET image, I_f is the intensity in the FRET-channel, I_{dd} is the intensity in the donor-channel, and I_{aa} is the intensity in the acceptor-channel.

Through imaging donor-acceptor fusion constructs of differing, but constant, FRET efficiencies, it is possible to calculate two proportionality constants that enable the calculation of FRET efficiencies for any single-chain biosensor (36). The G factor is calculated as:

$$G = -\frac{\Delta\left(\frac{F_c}{I_{aa}}\right)}{\Delta\left(\frac{I_{dd}}{I_{aa}}\right)} \quad (2)$$

where Δ indicates the change between two donor-acceptor fusion proteins.

The k factor is calculated as

$$k = \frac{I_{dd} + \frac{F_c}{G}}{I_{aa}} \quad (3)$$

With these two proportionality constants, it is possible to calculate both FRET efficiency (E) and the relative concentration of donor and acceptor fluorescent proteins $\frac{[D]}{[A]}$ in a sample:

$$E = \frac{\frac{F_c}{G}}{I_{dd} + \frac{F_c}{G}} \quad (4)$$

$$\frac{[D]}{[A]} = \frac{I_{dd} + \frac{F_c}{G}}{I_{aa}k} \quad (5)$$

To empirically calculate the G factor, distributions of acceptor-normalized corrected FRET (F_c/I_{aa}) and acceptor-normalized donor (I_{dd}/I_{aa}) were compiled from all pixels for each construct (GGS2 and TRAF) for a single experiment. Relevant pixels were isolated by manual cell masking. The mean, median, and mode of F_c/I_{aa} vs. I_{dd}/I_{aa} was determined for GGS2 and TRAF. The G factor was calculated as the slope of the line connecting each set of points, which stems from equation (2). A single day of imaging GGS2 and TRAF yields a single estimate of the G factor, and a total of four independent experiments were conducted. The data from the four independent experiments were also used to estimate the k factor as defined in equation (3). The k factor was calculated pixel-by-pixel, and the distribution of

the pixels for each construct (GGS2 and TRAF) was compiled. The k factor was estimated using either the mean, median, or mode of these distributions.

All symbols used in these calculations have been summarized in Supp. Table 3.

Automated Image Analysis

Custom written MATLAB (Mathworks) software was used for all image analysis. To identify single cells on an image, closed boundaries were drawn by the user based on the unmasked acceptor channel image. Information outside cell boundaries was discarded. For VinTS and VinTS-I997A images, FAs were identified in the acceptor channel, which is proportional to sensor concentration. Specifically, the FAs were segmented using the water algorithm, as previously described (14, 33, 41, 43, 48). The result of the FA segmentation was output as a binary mask, which was then applied across all images resulting from FRET analysis for visualization of data.

For each cell, FRET efficiency was characterized using the mean of the bootstrapped mode, a metric previously validated for characterizing biological data (49). Per common bootstrapping techniques (50), pixels within a cell were randomly sampled with replacement and the sample mode was estimated using the half-range mode algorithm (49). This step was reiterated 1,000 times to generate a distribution of the estimated mode for each cell's FRET efficiency. The mean of this distribution, referred to as the mean of the bootstrapped mode, was used to characterize FRET efficiency for each cell. For TSMod, only pixels isolated by manual cell masking were sampled. For VinTS-I997A and VinTS, pixels masked by both focal adhesion masking and manual cell masking were sampled. The sample size corresponded to the number of pixels within each analyzed cell. Note, the mean of the bootstrapped mode provides a single data point for each cell's FRET efficiency. An analogous procedure was conducted to determine the donor-per-acceptor value for each cell. Cells with a donor-per-acceptor value smaller than 0.5 or greater than 1.5 were excluded from subsequent analysis. In comparing populations of cells, common statistical techniques were used to compare each population of data points (Figs. 4–6).

Analysis of FRET Efficiency Uncertainty

To estimate the uncertainty of FRET efficiency measurements based on the experimental sample size, we randomly drew samples from our large datasets. This approach assumes that the complete dataset, consisting of hundreds of cells, accurately reflects the true distribution of the underlying population. Specifically, at each sample size (1–150 cells), the data was randomly sampled with replacement from each population, and the sample mean was calculated for a total of 10,000 iterations per sample size. Thus, a distribution of the sample mean was generated for each sample size. The uncertainty was defined as the width of the 95% confidence interval of this distribution for each sample size.

Statistics

Statistical analyses were performed using the software JMP Pro 13 (SAS, Cary, NC) or RStudio (Version 1.0.136). Comparisons of data with equal variances, as determined with Levene's test, were analyzed with an ANOVA and, if necessary, Tukey's HSD tests. Datasets

with unequal variances were analyzed with the non-parametric Welch's ANOVA and, if necessary, Games-Howell tests. A p value of $p < 0.05$ was considered statistically significant.

Code Availability

All code is available upon request.

Results:

Converting measurements of sensitized emission to FRET efficiency

A key step in the use of sensitized emission methods to quantify FRET efficiency for single-chain biosensors is the determination of four calibration factors (36, 40). The first two are used to correct for the bleedthrough of emission of the donor and acceptor fluorophores into the FRET channel. These two corrections are commonly used in the context of FRET indices (24, 25), and methods for their determination are relatively standard (11, 30). The third factor, typically termed G, represents a ratio of the acceptor emission in the FRET channel to the amount of donor emission in the donor channel for equimolar concentrations of excited donor and acceptor fluorophores, such as the case for single chain biosensors (36, 51). These three parameters are used to convert sensitized emission images, taken in the donor, FRET, and acceptor channels, into FRET efficiency. The fourth factor, k, represents the fluorescence intensity ratio between the donor and acceptor, at equimolar concentrations, in the absence of FRET (36). This parameter can be used to calculate an estimate of the ratio of the concentrations of the donor and acceptor, which enables measurements of fluorophore stoichiometry. For single-chain biosensors, the ratio should be unity. Notably, all calibration factors are fluorophore-, instrument-, and setting-dependent (36).

G and k can be determined with a single imaging setup and do not require FLIM or another technique to provide further information (36). To do so, two constructs with two different, but constant, FRET efficiencies are separately expressed in cells and imaged. The difference in FRET between the two constructs, due to the differences in their linker lengths, should be as wide as possible to improve the estimation(36). In this work, constructs consisted of mTFP1 and Venus (A206K), which correspond to the FRET pair used in VinTS (14). These fluorophores were chosen due to their improved brightness and photostability (52, 53), as compared to other genetically encoded fluorescent proteins, and suitability for FRET (54). To create a high FRET construct, the short flexible linker 2x(GGSGGS), which we denote as GGS2, was utilized (33). To create a low FRET construct, a derivative of tumor necrosis factor alpha (TNFα) receptor associated factor (TRAF) was used as has been done previously (36, 43, 45). The constructs mTFP1-GGS2-Venus and mTFP1-TRAF-Venus were separately expressed in vinculin −/− mouse embryonic fibroblasts (MEFs). Cells were imaged according to the details in Materials and Methods. Following acquisition of sensitized emission images, the donor (I_{dd}), bleedthrough-corrected FRET (F_c), and acceptor (I_{aa}) images were used to calculate acceptor-normalized corrected FRET (F_c/I_{aa}) and acceptor-normalized donor (I_{dd}/I_{aa}) intensities (Fig. 1A–B), which are used to estimate G. We later confirmed that GGS2 and TRAF resulted in significantly different FRET efficiencies as expected (Supp. Fig. 1).

To identify single cells in an image, closed boundaries were manually drawn based on the unmasked acceptor channel image. Information outside cell boundaries was discarded. Previous work using this method estimated the G and k factors using a cell-averaged approach (43). This approach, however, was sensitive to outliers and required user-defined selection criteria to reproducibly estimate the calibration factors. Therefore, we sought a robust, unbiased approach for precisely estimating the calibration factors required for calculating FRET efficiency from sensitized emission.

Mode-based numerical approach for determining calibration factors

Because microscope calibrations, such as spectral bleedthrough corrections, are measured pixel-by-pixel (11), we reasoned that a pixel-based approach might provide a precise, automated method for estimating the sensitized emission calibration factors. A sample density plot of all pixels, compiled from a single experiment, of acceptor-normalized corrected FRET (F_c/I_{aa}) versus the acceptor-normalized donor (I_{dd}/I_{aa}) is shown for GGS2 and TRAF (Fig. 1C). The data from both constructs is non-Gaussian and skewed toward the origin, suggesting the mean, median, and mode are likely to yield different values (55). Therefore, we examined which metric of the distribution average led to the most robust estimation of the calibration factors. While calculating the mean and median is straightforward, various methods exist to approximate the mode of a continuous distribution (49). Here, the half-range mode algorithm(56) was used because it does not require user input, such as bin size specification, and has previously been established as a suitable method for analyzing biological data (49). The half-range mode algorithm is an iterative process whereby a dataset is split into two groups based on the midpoint of the dataset's range (Supp. Fig. 2). The group with more points is identified and subsequently split based on the midpoint of its range. This process of estimating smaller intervals continues until only two points remain. The estimated mode is equal to the mean of these two points. For each experiment, the distribution average was determined for both GGS2 and TRAF using the mean, median, and mode. Then for each metric, the slope of the line connecting the two data points provided an estimate of G. Estimates of G were separately measured across four independent experiments (GGS2: n = 207 total cells; TRAF: n = 152 total cells), and the use of the three metrics to estimate G were compared (Fig. 1D).

Although statistical tests could not detect differences between the results of the various methods, the mode-based calculation of the G-factor (mean = 2.10, se = 0.026) was the most precise. In comparison, the mean- (mean = 2.61, se = 0.377) and median-based (mean = 2.29, se = 0.132) approaches both had significantly larger standard error (Fig. 1D). Comparison of these calculations to our previously published cell-averaged method (43) (mean = 2.25, se = 0.155) demonstrates that the mode-based estimation provides similar results to our previous approach without the need for user-defined exclusion criteria used in the previous work.

Using the refined estimate of G (2.10), the data pertaining to mTFP1-GGS2-Venus and mTFP1-TRAF-Venus was further analyzed to calculate the k factor (Fig. 2A) according to equation (3) described in the Materials and Methods. The distributions of the k factor for both GGS2 and TRAF were compiled from all pixels across a single experiment and appear

non-Gaussian (Fig. 2B). To determine which metric provides the most precise estimation of k, the distribution average was characterized using the mean, median, and mode. Across four independent experiments, this analysis yielded eight estimates of k for each of the three metrics. The comparisons (Fig. 2C) show that the three metrics, as well as the cell-averaged approach, provide estimates that are nearly equivalent.

Together, these results demonstrate that the mode is a precise, robust metric to estimate the calibration factors for sensitized emission-based FRET efficiency measurements and does not require user-determined exclusion of outliers. We note that these approaches are more critical in the determination of G than k. We speculate this difference exists because the calculation of G involves interpolating data from multiple constructs, whereas k can be determined from a single construct. Thus, G may be more sensitive to outliers, and the mode provides a robust quantification of the key distributions.

Mode-based characterization of FRET efficiency within a cell

Next, we tested whether a mode-based approach could better characterize FRET efficiency within a single cell. To begin, we examined a construct, specifically an unloaded tension sensor module (TSMod), that is expected to exhibit a single, normally distributed FRET efficiency. When TSMod is expressed in the cytosol of vinculin −/− MEFs, a characteristic FRET efficiency of approximately 28.6% has previously been observed (43). To characterize a cell's FRET efficiency distribution, we examined the mean, median, and mode. Due to the limited number of pixels per cell, however, we also tested whether bootstrapping would reduce the potential effect of noise, as recommended elsewhere (49). We note bootstrapping is a commonly used method for estimating properties of a statistic, such as the mean, median, or mode (50). Briefly, a sampling distribution of the statistic is determined by randomly resampling the data, and the bootstrap estimate of the parameter is the mean of the statistic from the bootstrapped samples (57). See Materials and Methods for additional details on this analysis. Comparison of over 400 cells individually characterized using the mean-, median-, and mode, both with and without bootstrapping, demonstrates that using the bootstrapped mode results in a population average that most closely matches the estimate from previous work (43) but without the use of user-defined exclusion criteria (Fig. 3). These findings demonstrate that, across a large population of cells, the bootstrapped mode provides an accurate, robust characterization of a cell's FRET efficiency distribution.

FRET-based tension sensor modules are insensitive to fixation

To begin to leverage the enhanced accuracy of the mode-based characterization, we chose to more thoroughly examine whether FRET-based tension sensors are compatible with traditional molecular biology techniques. While FRET-based tension sensors have been used extensively in live cells, it would be useful to combine them with other molecular assays, such as immunofluorescence (58) or proximity ligation assays (59), but these techniques commonly involve cell fixation and membrane permeabilization.

Fixation is known to have context-specific effects on fluorophores, as certain fixation protocols can quench fluorophores or significantly alter FRET measurements (36, 60–64). Common fixation protocols use paraformaldehyde (PFA) or methanol to physically cross-

link the constituents of the cell. Methanol, however, is inherently incompatible with FRET-based tension sensors because it leads to the denaturation of fluorescent proteins (64). Thus, vinculin −/− MEFs expressing cytosolic TSMod (Fig. 4A) were imaged either live or following EM-grade PFA fixation (Fig. 4B–C). Analysis of hundreds of cells expressing TSMod demonstrate that the population's mean FRET efficiency of TSMod under live and fixed conditions is comparable at 28.4% and 28.7%, respectively (Fig. 4L). These more accurate mode-based characterizations suggest that fixation with PFA does not inherently compromise the module's fluorophores or separation distance when it is expressed in cells.

Protein-incorporated tension sensor modules are insensitive to fixation

We next determined if fixation affects the tension sensor module when it is incorporated into a protein such as VinTS, which consists of TSMod inserted between its head and tail domains. As VinTS bears actomyosin-generated forces and fixation could affect the actomyosin network, an unloaded control was first used to isolate the effects of fixation on TSMod when it is incorporated into vinculin and localized to FAs. The vinculin mutation I997A, which decreases vinculin's binding affinity to actin (15, 65), was used to generate the unloaded control, denoted VinTS-I997A (Fig. 4D). Previous work has shown that VinTS-I997A experiences no loads in live cells (41). The mean FRET efficiency of VinTS-I997A in live and fixed vinculin −/− MEFs (Fig. 4E–F) is 28.5% and 27.9%, respectively (Fig. 4L). Therefore, fixation does not appear to affect protein-incorporated, FA-localized TSMod in the absence of load.

VinTS (Fig. 4H) was next examined to determine whether fixation affects the actomyosin network or TSMod in the presence of load. In vinculin −/− MEFs expressing VinTS (Fig. 4I–J), the population's mean FRET efficiency for live and fixed conditions has values of 20.5% and 21.3%, respectively (Fig. 4L). Thus, our mode-based characterization suggests that FRET-based tension sensors are compatible with this fixation protocol.

FRET-based tension sensors are unperturbed by a common immunofluorescence protocol

As fixation alone has limited applications, we examined the compatibility of VinTS with immunofluorescence, used to detect the abundance and localization of proteins or specific post-translational modifications. A typical immunofluorescence experiment requires the completion of several steps: fixation, permeabilization, blocking, and immuno-labeling. Since none of these steps individually are useful, we examined if FRET efficiency of VinTS is changed at the end of an indirect immunofluorescence protocol. Permeabilization and blocking were conducted with Triton-X and 2% BSA due to their widespread use. VinTS was immunolabeled using a vinculin primary antibody, as we reasoned the close proximity was most likely to reveal complexities such as possible interactions between the antibody and tension sensor. To minimize intermolecular FRET between the tension sensor and fluorescently-labeled secondary antibody, Alexa Fluor 647 was chosen because its excitation spectra has minimal overlap with Venus' emission spectra. To isolate effects on the sensor itself and alterations in the actomyosin cytoskeleton, VinTS-I997A (Fig. 4G) and VinTS (Fig. 4K) were separately probed. For VinTS-I997A and VinTS, the population's mean FRET efficiency is 28.0% and 21.1%, respectively (Fig. 4L). These values demonstrate that this immunofluorescence protocol does not significantly affect VinTS measurements.

Measurable differences in intermolecular FRET controls

To assess the sensitivity of mode-based FRET characterization, we sought to distinguish differences in FRET signals between two similar, but structurally unique, FRET constructs. Specifically, we examined two common pairs of constructs used to measure intermolecular FRET. The first pair of constructs, termed internal controls, consist of vinculin with either mTFP1 or Venus in place of the tension sensor module (Fig. 5A) (14). The second set of constructs, termed dark mutant controls (Fig. 5B), consist of VinTS with a point mutation that disrupts the fluorescence of either the acceptor or donor (44). The dark mutants were generated as described in the Materials and Methods. Either the internal controls or the dark mutant controls were expressed, imaged, and analyzed (Fig. 5C–D). However, to accurately estimate the amount of intermolecular FRET occurring in VinTS, it is necessary to have both physiological expression levels and equimolar expression of the two constructs which make up each control pair. To overcome this technological challenge, cells with an acceptor intensity approximately half that of VinTS-expressing cells were selectively imaged. Further, equimolar expression of the two constructs was achieved by examining cells with a donor-per-acceptor ratio between 0.5 and 1.5. For both construct pairs, little intermolecular FRET is observed as expected (Fig. 5E). However, the internal controls (n = 24 cells, N = 3 independent experiments) exhibit a FRET efficiency that is statistically different from the dark mutants (n = 31 cells, N = 3 independent experiments). Thus, with a relatively small sample size, a difference in FRET efficiency of approximately 4% is distinguishable. These results suggest that the internal controls over-estimate the degree of intermolecular FRET that may occur in VinTS. This disparity is likely due to the structural differences in the two control pairs. The dark mutants are likely better controls because they more closely mimic the structure of VinTS.

Sample size affects uncertainty of FRET efficiency measurements

In recent FRET-based tension sensor studies (66–72), sample sizes have ranged from tens to hundreds, and statistics have been done on data that varies in length scale from sub-cellular structures to whole cells. Therefore, we investigated how sample size, specifically the number of cells analyzed, affects the uncertainty of FRET efficiency measurements. We focused on whole cell measurements so sensors that localize to the cytosol as well as FAs could be compared. We simulated experimental sampling to approximate the uncertainty, defined as the width of the 95% confidence interval of the sample mean, for a given sample size. Further details can be found in the Materials and Methods.

First, we examined data from live and fixed cells expressing TSMod. The curves pertaining to these conditions closely align, demonstrating that fixation does not alter the uncertainty of FRET measurements (Fig. 6A). Next, we evaluated the performance of TSMod, VinTS-I997A, and VinTS under live conditions (Fig. 6B). TSMod exhibits the least uncertainty at all sample sizes, and VinTS exhibits the most. This suggests that both incorporation of TSMod into a protein and being subjected to load may increase the uncertainty of FRET measurements. Thus, the uncertainty may also be dependent on the conditions experienced by the cells and/or cell-to-cell heterogeneity. Looking closer at these results, the uncertainty of TSMod is 1.9% and 1.1% when looking at 30 or 100 cells, respectively. Likewise, the uncertainty of VinTS is 3.1% and 1.7% for 30 and 100 cells, respectively. This demonstrates

that extra care should be taken when evaluating FRET-based tension sensor datasets of small size and small changes in tension. For our experimental setup, this analysis demonstrates that differences in roughly 1–2% FRET efficiency can be distinguished at large sample sizes. Differences smaller than this, however, appear unresolvable. This analysis serves as a valuable gauge and could be used as a rough indicator for when small samples are not indicative of population statistics. We suggest that researchers should use these insights and similar analyses to guide their own experimental design for studies involving FRET-based tension sensors.

Discussion:

Building on the previously established methods of using sensitized emission to calculate FRET efficiency (36, 40), this work described approaches for minimizing and quantifying variability in FRET calculations. To reduce the variability of FRET efficiency calculations, we first developed numerical methods to accurately calculate the necessary calibration factors. Our results demonstrated that a mode-based analysis of two control constructs exhibiting high and low FRET, termed GGS2 and TRAF, respectively, provided the most precise estimate of the G and k calibration factors. A similar mode-based approach was incorporated into the analysis of FRET-based tension sensors to increase the reliability and consistency of characterizing the molecular loads experienced by vinculin. While the intention of this paper was to improve FRET measurements of VinTS, our previous work has already validated the function of this sensor (14, 33, 41, 43). Notably, recent modeling efforts have described the effects of the rotational mobility of the fluorophores and the flexibility of the linker (33). The described mode-based approach was found to be less susceptible to noise and outliers than the mean-based approach which is most commonly used to characterize FRET-based tension sensor measurements (14, 20, 44, 66, 73). Although it was not explored in this work, the skewness in the FRET efficiency distributions, specifically for the cytosolic sensors, could be an interesting topic to explore. At this time, it is difficult to pinpoint a single mechanism for the skewness of the data from FRET-based biosensor experiments. Slight changes in the folding or functionality of a subset of the sensors, the localization of sensors within different sub-cellular compartments, or a variety of other variables could lead to changes that would affect the FRET. For this reason, we have chosen to focus on accurately estimating the mode of the FRET distributions, which, at sufficiently high signal to noise, is an accurate quantification of FRET. Furthermore, we note that demonstrating that previously developed control constructs (14, 43) report the expected FRET efficiency is a simple and powerful means to ensure that experimental conditions are achieving a sufficient signal to noise.

Using our robust characterization method, we further demonstrated that VinTS is unperturbed by several processing steps associated with immuno-labeling, namely fixation, permeabilization, blocking, and antibody labeling. This is significant because it suggests that future researchers can simultaneously measure molecular loads and conduct ancillary tests on the same sample. This type of insight will likely lead to a significant improvement in our understanding of mechanobiology and mechanosensitive processes (74). For example, one could examine how adhesion composition or signaling changes in response to load. However, we note that these results may not be generally applicable. Similar evaluations are

still necessary for FRET-based tension sensors used in other proteins and likely for VinTS if it is used in cells within different mechanical microenvironments, such as in 3D cell culture. It should also be noted that *in vivo* analyses, which are limited in sample size, may benefit from FLIM-based approaches because they don't require as many control constructs (75).

The sensitivity of the new method was tested by comparing the FRET efficiency of two similar, yet structurally distinct, intermolecular FRET controls. In addition to detecting a small difference in FRET efficiency between the two controls, we found that vinculin internal controls may over-estimate the amount of intermolecular FRET occurring in cells expressing VinTS. This demonstrates that dark mutants are a more appropriate intermolecular FRET control because they are nearly identical to the structure of the tension sensor itself. We also note that the cytosolic sensors, which include GGS2, TRAF, and TSMod, are unlikely to undergo intermolecular FRET because their acceptor intensity, an indication of concentration, is approximately equivalent to or less than the vinculin-based constructs. Previously, we had also shown that the FRET efficiency of cytosolic sensors is independent of sensor concentration at or below the observed expression levels (33).

Since the number of samples are often limited for complex biological experiments, we examined how sample size affects the uncertainty in our estimation of a population's mean FRET efficiency. For all constructs, we found that small sample sizes (< 30 cells) were associated with high uncertainty. As sample size increased, uncertainty reduced to an apparent limit of approximately 1–2% FRET efficiency. This suggests that differences below this amount are indeterminable. Furthermore, it emphasizes the benefits of rationally designed sensors that are optimally tuned for particular force regimens (33). We also discovered that uncertainty is dependent on experimental conditions or molecular loading. To obtain the large sample sizes required for this analysis, we used stable, as opposed to transient, expression of constructs. Although stable expression permits the selection of construct expression levels via cell sorting, there is a risk that homologous recombination may occur due to the sequence similarity of commonly used fluorescent proteins (76). To avoid homologous recombination, stable expression should be reserved for tension sensor modules consisting of fluorophores derived from different species, such as the mTFP1-Venus module used here, or sequences that have been codon-scrambled (76, 77).

To summarize, we showed that mode-based approaches improve the accuracy of both the microscope calibrations needed for sensitized emission-based FRET measurements as well as the measurement of a cell's average FRET efficiency. Additionally, we provided estimates that enable *a priori* estimates of the number of measurements needed to achieve a desired accuracy. These mode-based methods demonstrate VinTS measurements are compatible with immunolabeling techniques such as fluorescence co-localization and proximity ligation assays, suggesting other sensors may also be compatible with these commonly-used and powerful approaches. This opens the door for a host of possible experiments that could help researchers better understand the underlying mechanisms of mechanotransduction.

Supplementary Material

Refer to Web version on PubMed Central for supplementary material.

Acknowledgements:

The authors thank Dr. Ben Fabry and Dr. Wolfgang H Goldmann (Friedrich-Alexander-Universitat Erlangen-Nurnberg) for providing vinculin −/− cells. The authors also thank Dr. Chris Gilchrist and Timothy Curtis Shoyer for comments and examination of the manuscript.

Research support: Research reported in this publication was supported by the National Institute of General Medical Sciences (R01GM121739), National Institute of Biomedical Imaging and Bioengineering (R21EB022166), and Eunice Kennedy Shriver National Institute of Child Health and Human Development (R21HD084290) of the National Institutes of Health (NIH) through awards given to B.D.H. The content is solely the responsibility of the authors and does not necessarily represent the official views of the NIH. This research was also supported by the National Science Foundation (NSF) under Grant No. 14–54257 awarded to B.D.H. as well as the NSF Graduate Research Fellowship Program under Grant No. DGE-1644868 and DGF-1644868 awarded to E.M.G. and K.E.R., respectively. Any opinions, findings, and conclusions or recommendations expressed in this material are those of the authors and do not necessarily reflect the views of the NSF.

Literature Cited:

1. Chin LK, Xia YT, Discher DE, & Janmey PA (2016) Mechanotransduction in cancer. Curr Opin Chem Eng 11:77–84. [PubMed: 28344926]
2. Tabas I, Garcia-Cardena G, & Owens GK (2015) Recent insights into the cellular biology of atherosclerosis. J Cell Biol 209(1):13–22. [PubMed: 25869663]
3. Nikkhah M, Edalat F, Manoucheri S, & Khademhosseini A (2012) Engineering microscale topographies to control the cell-substrate interface. Biomaterials 33(21):5230–5246. [PubMed: 22521491]
4. Hoffman BD, Grashoff C, & Schwartz MA (2011) Dynamic molecular processes mediate cellular mechanotransduction. Nature 475(7356):316–323. [PubMed: 21776077]
5. Han MKL & de Rooij J (2016) Converging and Unique Mechanisms of Mechanotransduction At Adhesion Sites. Trends Cell Biol 26(8):612–623. [PubMed: 27036655]
6. Hoffman BD & Yap AS (2015) Towards a Dynamic Understanding of Cadherin-Based Mechanobiology. Trends Cell Biol 25(12):803–814. [PubMed: 26519989]
7. Alberts B, et al. (2015) Molecular Biology of the Cell, Sixth Edition. Molecular Biology of the Cell, Sixth Edition:1–1342.
8. Gayrard C & Borghi N (2016) FRET-based Molecular Tension Microscopy. Methods 94:33–42. [PubMed: 26210398]
9. LaCroix AS, Rothenberg KE, & Hoffman BD (2015) Molecular-Scale Tools for Studying Mechanotransduction. Annu Rev Biomed Eng 17:287–316. [PubMed: 26421895]
10. Hoffman BD (2014) The Detection and Role of Molecular Tension in Focal Adhesion Dynamics. Prog Mol Biol Transl 126:3–24.
11. LaCroix AS, Rothenberg KE, Berginski ME, Urs AN, & Hoffman BD (2015) Construction, imaging, and analysis of FRET-based tension sensors in living cells. Method Cell Biol 125:161–186.
12. Jurchenko C & Salaita KS (2015) Lighting Up the Force: Investigating Mechanisms of Mechanotransduction Using Fluorescent Tension Probes. Mol Cell Biol 35(15):2570–2582. [PubMed: 26031334]
13. Polacheck WJ & Chen CS (2016) Measuring cell-generated forces: a guide to the available tools. Nat Methods 13(5):415–423. [PubMed: 27123817]
14. Grashoff C, et al. (2010) Measuring mechanical tension across vinculin reveals regulation of focal adhesion dynamics. Nature 466(7303):263–266. [PubMed: 20613844]
15. Thievessen I, et al. (2013) Vinculin-actin interaction couples actin retrograde flow to focal adhesions, but is dispensable for focal adhesion growth. J Cell Biol 202(1):163–177. [PubMed: 23836933]
16. Case LB, et al. (2015) Molecular mechanism of vinculin activation and nanoscale spatial organization in focal adhesions. Nat Cell Biol 17(7):880–892. [PubMed: 26053221]

17. Riveline D, et al. (2001) Focal contacts as mechanosensors: Externally applied local mechanical force induces growth of focal contacts by an mDia1-dependent and ROCK-independent mechanism. J Cell Biol 153(6):1175–1185. [PubMed: 11402062]
18. Yonemura S, Wada Y, Watanabe T, Nagafuchi A, & Shibata M (2010) alpha-Catenin as a tension transducer that induces adherens junction development. Nat Cell Biol 12(6):533–U535. [PubMed: 20453849]
19. le Duc Q, et al. (2010) Vinculin potentiates E-cadherin mechanosensing and is recruited to actin-anchored sites within adherens junctions in a myosin II-dependent manner (vol 189, pg 1107, 2010). J Cell Biol 191(4):891–891.
20. Borghi N, et al. (2012) E-cadherin is under constitutive actomyosin-generated tension that is increased at cell-cell contacts upon externally applied stretch. Proc Natl Acad Sci U S A 109(31): 12568–12573. [PubMed: 22802638]
21. Cai DF, et al. (2014) Mechanical Feedback through E-Cadherin Promotes Direction Sensing during Collective Cell Migration. Cell 157(5):1146–1159. [PubMed: 24855950]
22. Eder D, Basler K, & Aegerter CM (2017) Challenging FRET-based E-Cadherin force measurements in Drosophila. Sci Rep-Uk 7.
23. Lakowicz JR (2006) Principles of fluorescence spectroscopy (Springer, New York) 3rd Ed pp xxvi, 954 p.
24. Berney C & Danuser G (2003) FRET or no FRET: a quantitative comparison. Biophys J 84(6): 3992–4010. [PubMed: 12770904]
25. Zeug A, Woehler A, Neher E, & Ponimaskin EG (2012) Quantitative intensity-based FRET approaches--a comparative snapshot. Biophys J 103(9):1821–1827. [PubMed: 23199910]
26. Zal T & Gascoigne NRJ (2004) Photobleaching-corrected FRET efficiency imaging of live cells (vol 86, pg 3923, 2003). Biophys J 87(4):2915–2915.
27. Pertz O, Hodgson L, Klemke RL, & Hahn KM (2006) Spatiotemporal dynamics of RhoA activity in migrating cells. Nature 440(7087):1069–1072. [PubMed: 16547516]
28. Chen H, Cohen DM, Choudhury DM, Kioka N, & Craig SW (2005) Spatial distribution and functional significance of activated vinculin in living cells. J Cell Biol 169(3):459–470. [PubMed: 15883197]
29. Kim TJ, et al. (2015) Dynamic visualization of alpha-catenin reveals rapid, reversible conformation switching between tension states. Curr Biol 25(2):218–224. [PubMed: 25544608]
30. Hodgson L, Shen F, & Hahn K (2010) Biosensors for characterizing the dynamics of rho family GTPases in living cells. Curr Protoc Cell Biol Chapter 14:Unit 14 11 11–26.
31. Vogel SS, van der Meer BW, & Blank PS (2014) Estimating the distance separating fluorescent protein FRET pairs. Methods 66(2):131–138. [PubMed: 23811334]
32. Freikamp A, Cost AL, & Grashoff C (2016) The Piconewton Force Awakens: Quantifying Mechanics in Cells. Trends Cell Biol 26(11):838–847. [PubMed: 27544876]
33. LaCroix AS, Lynch AD, Berginski ME, & Hoffman BD (2018) Tunable molecular tension sensors reveal extension-based control of vinculin loading. Elife 7.
34. Meng F, Suchyna TM, Lazakovitch E, Gronostajski RM, & Sachs F (2011) Real Time FRET Based Detection of Mechanical Stress in Cytoskeletal and Extracellular Matrix Proteins. Cell Mol Bioeng 4(2):148–159. [PubMed: 21625401]
35. Wallrabe H & Periasamy A (2005) Imaging protein molecules using FRET and FLIM microscopy. Curr Opin Biotechnol 16(1):19–27. [PubMed: 15722011]
36. Chen H, Puhl HL, Koushik SV, Vogel SS, & Ikeda SR (2006) Measurement of FRET efficiency and ratio of donor to acceptor concentration in living cells. Biophys J 91(5):L39–L41. [PubMed: 16815904]
37. Leavesley SJ & Rich TC (2016) Overcoming limitations of FRET measurements. Cytometry A 89(4):325–327. [PubMed: 27101317]
38. Pietraszewska-Bogiel A & Gadella TWJ (2011) FRET microscopy: from principle to routine technology in cell biology. J Microsc-Oxford 241(2):111–118.
39. Leavesley SJ, Britain AL, Cichon LK, Nikolaev VO, & Rich TC (2013) Assessing FRET using spectral techniques. Cytometry A 83(10):898–912. [PubMed: 23929684]

40. Hoppe A, Christensen K, & Swanson JA (2002) Fluorescence resonance energy transfer-based stoichiometry in living cells. Biophys J 83(6):3652–3664. [PubMed: 12496132]
41. Rothenberg KE, Scott DW, Christoforou N, & Hoffman BD (2018) Vinculin Force-Sensitive Dynamics at Focal Adhesions Enable Effective Directed Cell Migration. Biophys J 114(7):1680–1694. [PubMed: 29642037]
42. Nagy P, et al. (2014) Maximum likelihood estimation of FRET efficiency and its implications for distortions in pixelwise calculation of FRET in microscopy. Cytometry A 85(11):942–952. [PubMed: 25123296]
43. Rothenberg KE, Neibart SS, LaCroix AS, & Hoffman BD (2015) Controlling Cell Geometry Affects the Spatial Distribution of Load Across Vinculin. Cell Mol Bioeng 8(3):364–382.
44. Conway DE, et al. (2013) Fluid shear stress on endothelial cells modulates mechanical tension across VE-cadherin and PECAM-1. Curr Biol 23(11):1024–1030. [PubMed: 23684974]
45. Koushik SV, Chen H, Thaler C, Puhl HL, & Vogel SS (2006) Cerulean, Venus, and Venus(Y67C) FRET reference standards. Biophysical Journal 91(12):L99–L101. [PubMed: 17040988]
46. Mierke CT, et al. (2010) Vinculin facilitates cell invasion into three-dimensional collagen matrices. The Journal of biological chemistry 285(17):13121–13130. [PubMed: 20181946]
47. LaCroix AS, Rothenberg KE, Berginski ME, Urs AN, & Hoffman BD (2015) Construction, imaging, and analysis of FRET-based tension sensors in living cells. Methods in cell biology 125:161–186. [PubMed: 25640429]
48. Zamir E, et al. (1999) Molecular diversity of cell-matrix adhesions. Journal of cell science 112 (Pt 11):1655–1669. [PubMed: 10318759]
49. Hedges SB & Shah P (2003) Comparison of mode estimation methods and application in molecular clock analysis. Bmc Bioinformatics 4.
50. Efron B & Tibshirani R (1993) An introduction to the bootstrap (Chapman & Hall, New York) pp xvi, 436 p.
51. Tron L, et al. (1984) Flow cytometric measurement of fluorescence resonance energy transfer on cell surfaces. Quantitative evaluation of the transfer efficiency on a cell-by-cell basis. Biophys J 45(5):939–946. [PubMed: 6428482]
52. Nagai T, et al. (2002) A variant of yellow fluorescent protein with fast and efficient maturation for cell-biological applications. Nat Biotechnol 20(1):87–90. [PubMed: 11753368]
53. Ai HW, Henderson JN, Remington SJ, & Campbell RE (2006) Directed evolution of a monomeric, bright and photostable version of Clavularia cyan fluorescent protein: structural characterization and applications in fluorescence imaging. Biochem J 400(3):531–540. [PubMed: 16859491]
54. Day RN, Booker CF, & Periasamy A (2008) Characterization of an improved donor fluorescent protein for Forster resonance energy transfer microscopy. J Biomed Opt 13(3):031203. [PubMed: 18601527]
55. Dalenius T (1965) The Mode - a Neglected Statistical Parameter. J R Stat Soc Ser a-G 128(1):110–117.
56. Bickel DR (2002) Robust estimators of the mode and skewness of continuous data. Comput Stat Data An 39(2):153–163.
57. Quinn GP & Keough MJ (2002) Experimental design and data analysis for biologists (Cambridge University Press, Cambridge, UK; New York) pp xvii, 537 p.
58. Donaldson JG (2001) Immunofluorescence staining. Curr Protoc Cell Biol Chapter 4:Unit 4 3.
59. Greenwood C, et al. (2015) Proximity assays for sensitive quantification of proteins. Biomol Detect Quantif 4:10–16. [PubMed: 27077033]
60. Anikovsky M, Dale L, Ferguson S, & Petersen N (2008) Resonance energy transfer in cells: a new look at fixation effect and receptor aggregation on cell membrane. Biophys J 95(3):1349–1359. [PubMed: 18359791]
61. Rodighiero S, et al. (2008) Fixation, mounting and sealing with nail polish of cell specimens lead to incorrect FRET measurements using acceptor photobleaching. Cell Physiol Biochem 21(5–6):489–498. [PubMed: 18453757]

62. Malkani N & Schmid JA (2011) Some secrets of fluorescent proteins: distinct bleaching in various mounting fluids and photoactivation of cyan fluorescent proteins at YFP-excitation. Plos One 6(4):e18586. [PubMed: 21490932]
63. Joosen L, Hink MA, Gadella TW, Jr., & Goedhart J (2014) Effect of fixation procedures on the fluorescence lifetimes of Aequorea victoria derived fluorescent proteins. J Microsc 256(3):166–176. [PubMed: 25179491]
64. Brock P, Hamelers IHL, & Jovin TM (1999) Comparison of fixation protocols for adherent cultured cells applied to a GFP fusion protein of the epidermal growth factor receptor. Cytometry 35(4):353–362. [PubMed: 10213201]
65. Thompson PM, et al. (2014) Identification of an actin binding surface on vinculin that mediates mechanical cell and focal adhesion properties. Structure 22(5):697–706. [PubMed: 24685146]
66. Ringer P, et al. (2017) Multiplexing molecular tension sensors reveals piconewton force gradient across talin-1. Nat Methods 14(11):1090-+. [PubMed: 28945706]
67. Papadopulos A, et al. (2015) Activity-driven relaxation of the cortical actomyosin II network synchronizes Munc18–1-dependent neurosecretory vesicle docking. Nat Commun 6.
68. Kuriyama S, et al. (2014) In vivo collective cell migration requires an LPAR2-dependent increase in tissue fluidity. J Cell Biol 206(1):113–127. [PubMed: 25002680]
69. Gayrard C, Bernaudin C, Dejardin T, Seiler C, & Borghi N (2018) Src- and confinement-dependent FAK activation causes E-cadherin relaxation and beta-catenin activity. J Cell Biol 217(3):1063–1077. [PubMed: 29311227]
70. Ron A, et al. (2017) Cell shape information is transduced through tension-independent mechanisms. Nat Commun 8.
71. Sarangi BR, et al. (2017) Coordination between Intra- and Extracellular Forces Regulates Focal Adhesion Dynamics. Nano Lett 17(1):399–406. [PubMed: 27990827]
72. Sigaut L, et al. (2018) Live cell imaging reveals focal adhesions mechanoresponses in mammary epithelial cells under sustained equibiaxial stress. Sci Rep 8(1):9788. [PubMed: 29955093]
73. Krieg M, Dunn AR, & Goodman MB (2014) Mechanical control of the sense of touch by beta-spectrin. Nat Cell Biol 16(3):224–233. [PubMed: 24561618]
74. Morimatsu M, Mekhdjian AH, Chang AC, Tan SJ, & Dunn AR (2015) Visualizing the Interior Architecture of Focal Adhesions with High-Resolution Traction Maps. Nano Lett 15(4):2220–2228. [PubMed: 25730141]
75. Lagendijk AK, et al. (2017) Live imaging molecular changes in junctional tension upon VE-cadherin in zebrafish. Nat Commun 8(1):1402. [PubMed: 29123087]
76. Komatsubara AT, Matsuda M, & Aoki K (2015) Quantitative analysis of recombination between YFP and CFP genes of FRET biosensors introduced by lentiviral or retroviral gene transfer. Sci Rep-Uk 5.
77. Tang NC & Chilkoti A (2016) Combinatorial codon scrambling enables scalable gene synthesis and amplification of repetitive proteins. Nat Mater 15(4):419–424. [PubMed: 26726995]

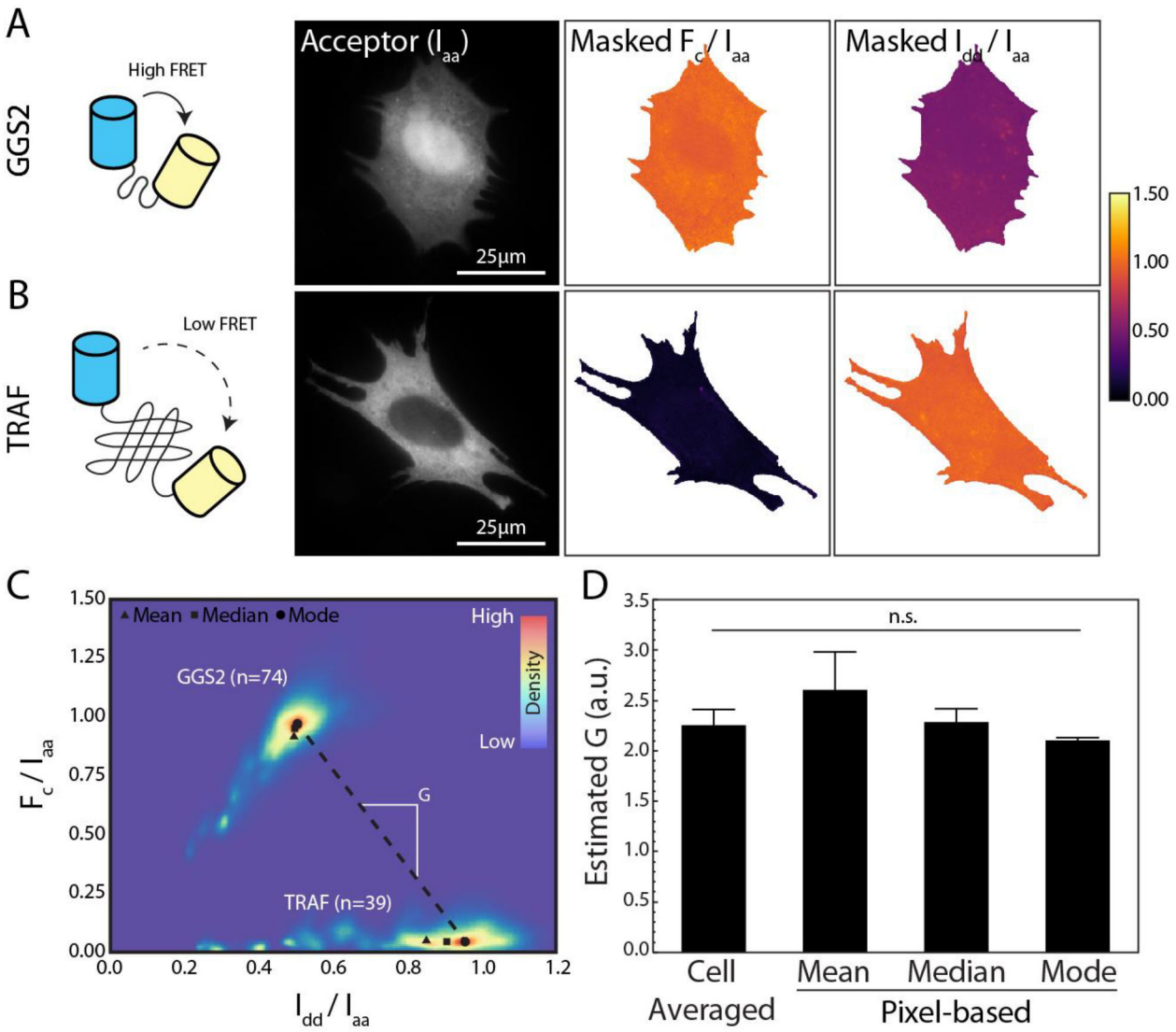

Figure 1.

(**A**) A cytosolic module consisting of mTFP1 (blue) linked to Venus (yellow) via a glycine-glycine-serine repeat (GGS2), which results in high FRET due to the short linker length. (**B**) A cytosolic module consisting of mTFP1 (blue) linked to Venus (yellow) via a derivative of tumor necrosis factor alpha (TNFα) receptor associated factor (TRAF), which results in low FRET due to the long linker length. Localization of the constructs in vinculin −/− MEFs is shown in the acceptor channel (I_{aa}). The corresponding acceptor-normalized corrected-FRET (F_c/I_{aa}) image and acceptor-normalized donor (I_{dd}/I_{aa}) image are shown with pseudo-coloring. (**C**) Heatmap of F_c/I_{aa} vs. I_{dd}/I_{aa} pixel data used to estimate the G factor. Data comes from all pixels segmented by cell masks for GGS2 (n = 74 cells) and TRAF (n = 39 cells) from a single experiment. Triangles, squares, and circles used to denote the mean, median, and mode, respectively, of each population, and the slope of the black dashed line corresponds to the estimation of G based on the mode. (**D**) Comparison of the four methods used to estimate G. Methods include a previously described cell-averaged approach (43) and our newer pixel-based approach using the mean, median, or mode. Data and error bars are

the mean and standard error, respectively, from four independent experiments. Due to unequal variances as determined by the Levene's test, Welch's ANOVA was used and a statistically significant difference in means was not found.

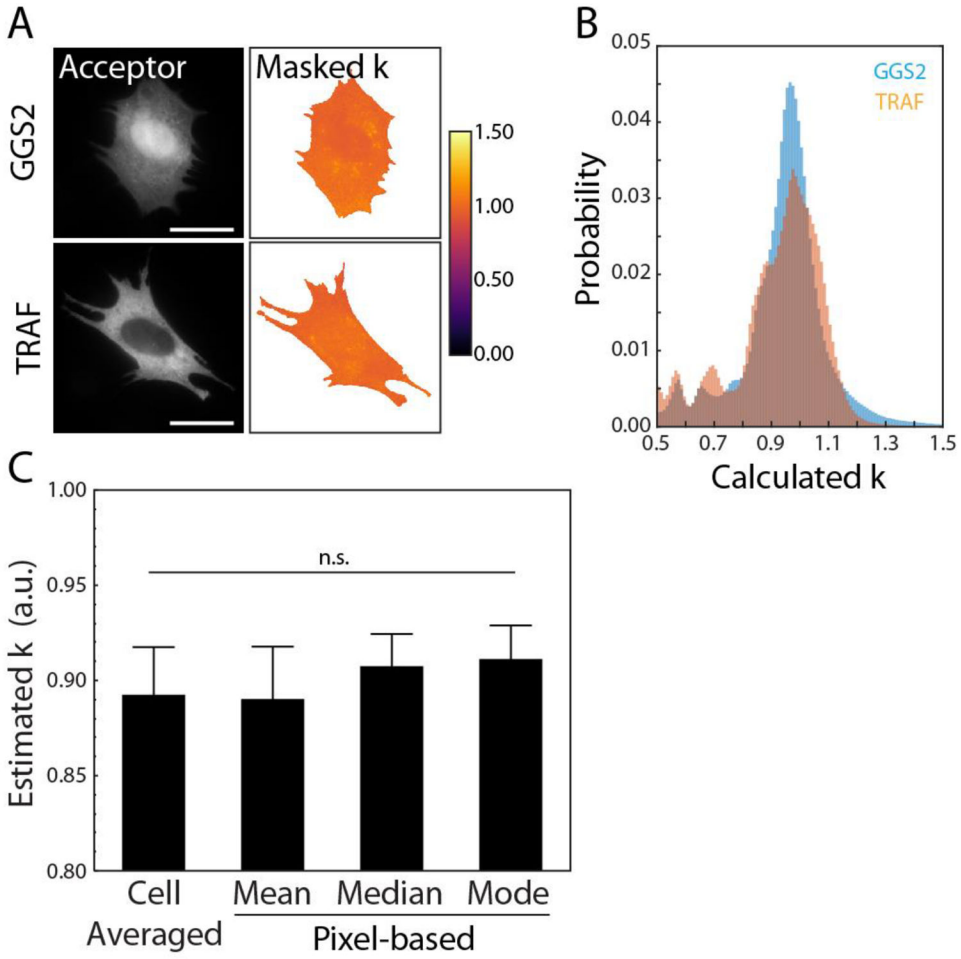

Figure 2.

(**A**) Sample acceptor images of vinculin −/− MEFs expressing either GGS2 or TRAF and the associated cell-masked, pseudo-colored images of the calculated k factor. Scale bars are 25μm. (**B**) Histogram of pixel data corresponding to either GGS2 (blue, n = 74 cells) or TRAF (orange, n = 39 cells) from all cells in a single experiment. (**C**) Comparison of the four methods used to estimate k. Methods include a previously described cell-averaged approach (43) and our pixel-based approach using the mean, median, or mode. Data and error bars are the mean and standard error, respectively, from both constructs across four independent experiments. Following a Levene's test, an ANOVA did not find statistically significant differences in the means.

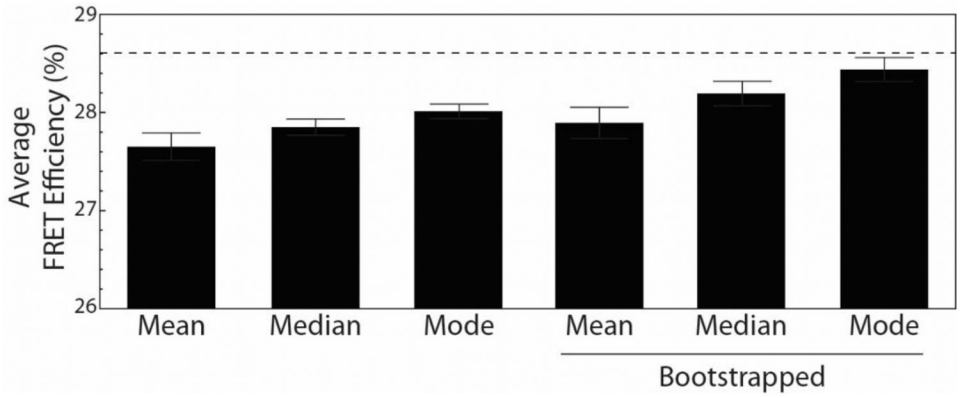

Figure 3.

Comparison of different methods to characterize FRET efficiency in live, TSMod-expressing vinculin −/− MEFs. For each cell, the FRET efficiency was characterized from either the mean, median, or mode, with and without bootstrapping. Data and error bars are the mean and standard error, respectively, of the entire cell population (n = 454 cells, N = 11 experiments). Dashed line represents a published FRET efficiency value of 28.6% for unloaded mTFP1-$(GPGGA)_8$-Venus (TSMod) (43).

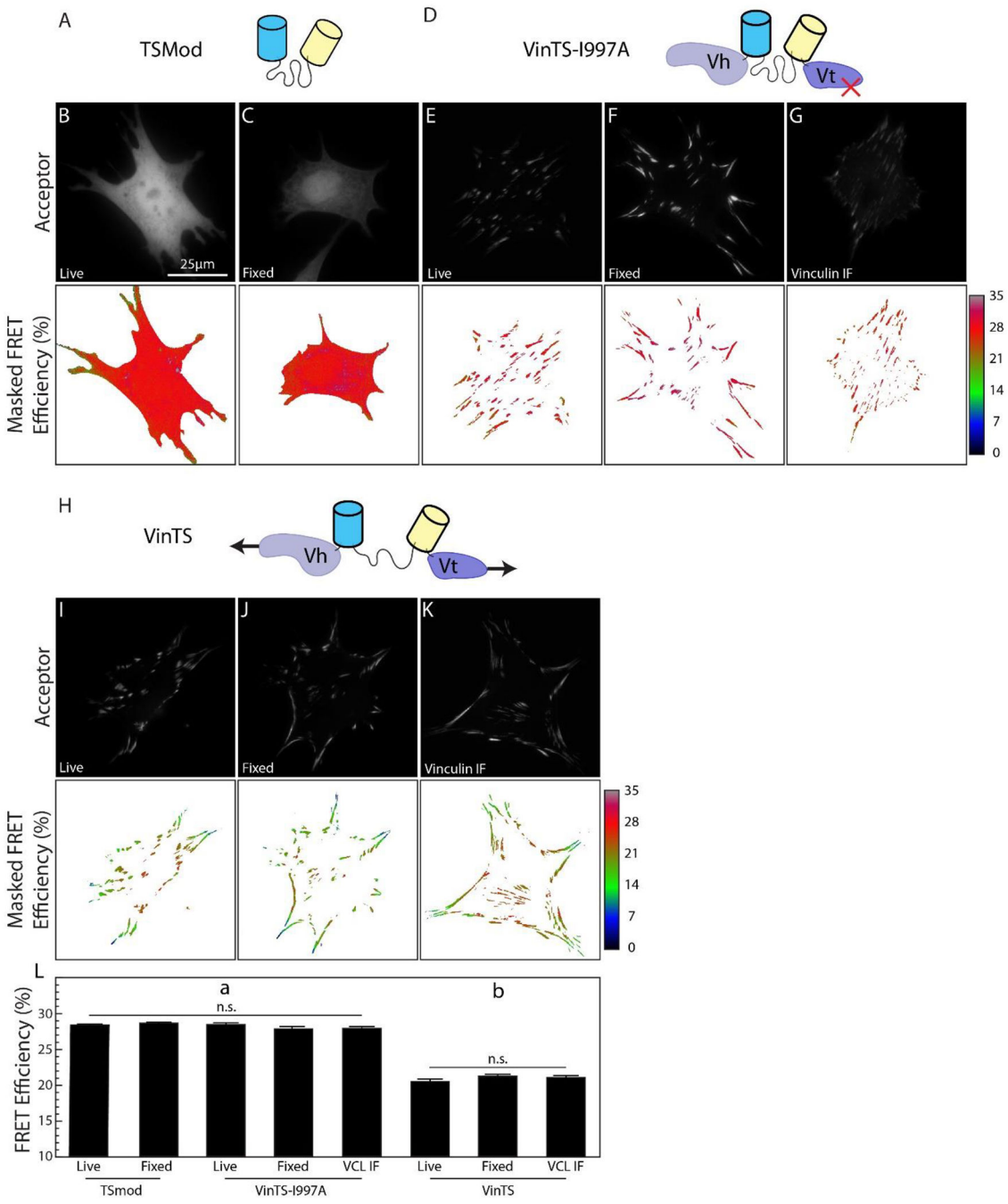

Figure 4.

(**A**) The tension sensor module (TSMod) consists of two fluorophores separated by a flagelliform linker sequence $(GPGGA)_8$. Localization and estimated FRET efficiency of TSMod in (**B**) live and (**C**) paraformaldehyde-fixed vinculin −/− MEF cells. (**D**) The actin-binding vinculin tension sensor mutant (VinTS-I997A) consists of TSMod inserted after aa 883 of vinculin and a point mutation at aa 997. Localization and estimated FRET efficiency of VinTS-I997A in (**E**) live, (**F**) paraformaldehyde-fixed, and (**G**) vinculin immunofluorescently-labeled vinculin −/− MEFs. (**H**) The vinculin tension sensor (VinTS)

consists of TSMod inserted after aa 883. Localization and estimated FRET efficiency of VinTS in (**I**) live, (**J**) paraformaldehyde-fixed, and (**K**) vinculin immunofluorescently-labeled vinculin −/− MEFs. FRET distributions of all sample images are provided in Supp. Fig. 3. (**L**) Mean FRET efficiency of TSMod (live, n = 454, N = 11; fixed, n = 378, N = 11), VinTS-I997A (live, n = 161, N = 11; fixed, n = 50, N = 2; Vinculin IF, n = 272, N = 5), and VinTS (live, n = 173, N = 13; fixed, n = 164, N = 6; vinculin IF, n = 98, N = 3) under various conditions. Following a Levene's test, differences between (a) TSMod and VinTS-I997A and (b) VinTS was determined by a Welch's ANOVA and Games-Howell Test. Error bars represent one standard error.

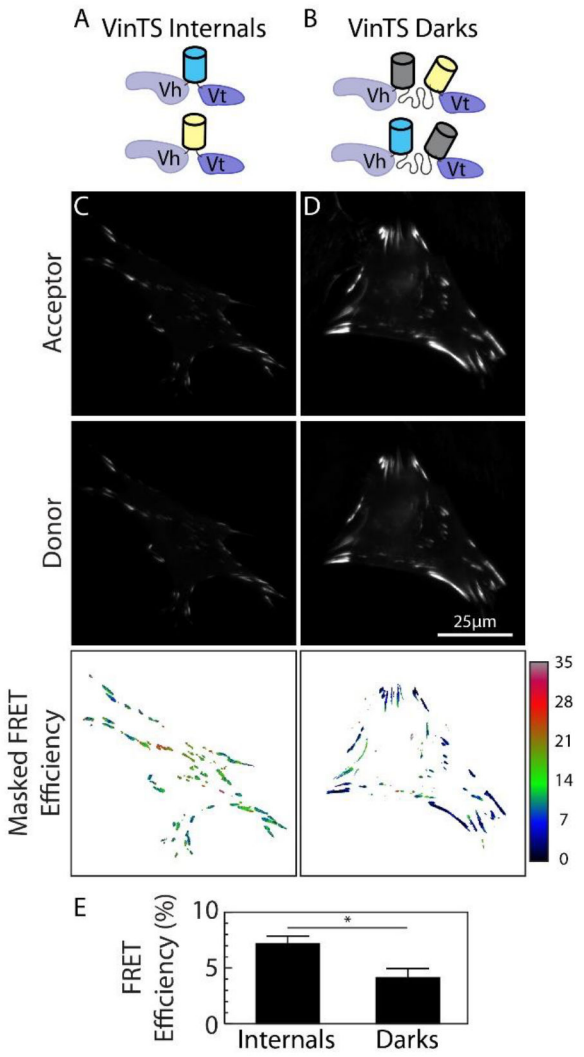

Figure 5.

(**A**) Internal vinculin intermolecular FRET controls contain Venus or mTFP1 inserted at aa 883. (**B**) VinTS dark intermolecular FRET controls contain point mutations on either Venus or mTFP1 that disrupt the fluorescent properties of the fluorophore. (**C**) Localization of internal vinculin constructs co-expressed in a vinculin −/− MEF. (**D**) Localization of VinTS dark constructs co-expressed in a vinculin −/− MEF. The corresponding masked FRET efficiencies are also shown. (**E**) Difference in the mean FRET efficiency of vinculin internals and VinTS darks determined by t-test ($p = 0.0014$). Error bars are one standard error.

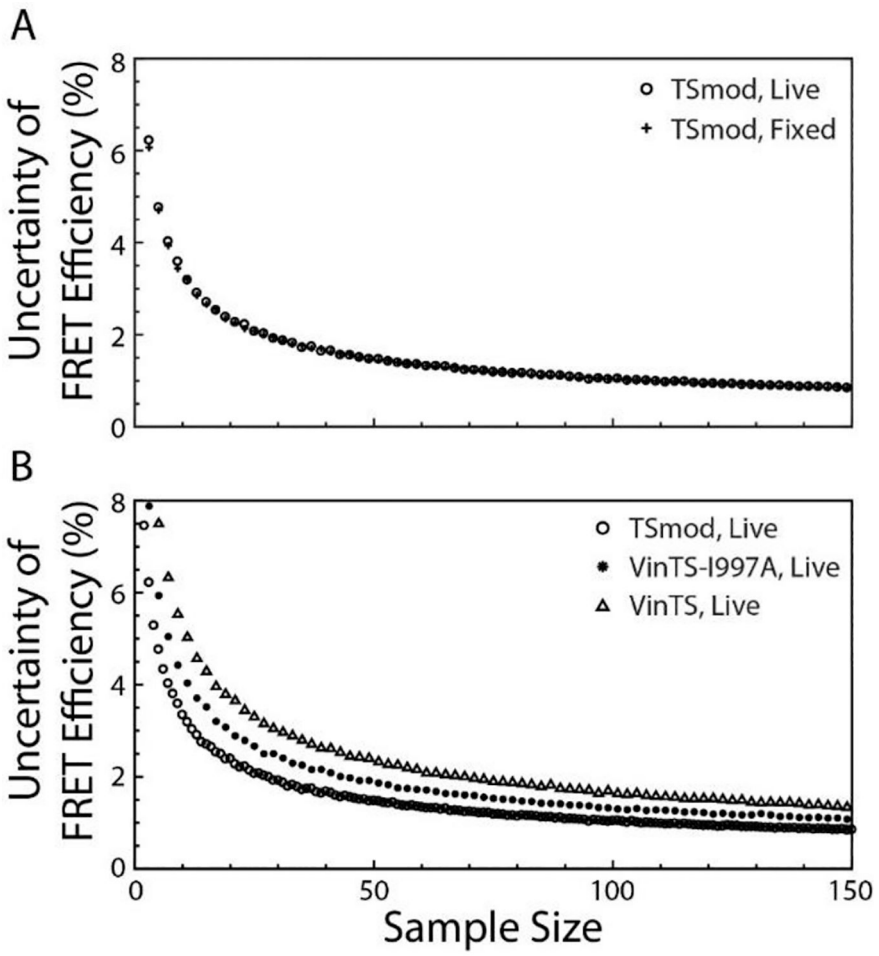

Figure 6.

(**A**) Uncertainty in the estimation of the population's mean FRET efficiency as a function of sample size for TSMod expressed in live (n = 454) and fixed (n = 378) vinculin −/− MEFs. For each sample size, the uncertainty is the width of the 95% confidence interval of the mean's distribution, which arises from the simulated experimental sampling explained in the Materials & Methods. (**B**) The same analysis was performed on data from live vinculin −/− MEFs expressing either TSMod (n = 454), VinTS-I997A (n = 161), or VinTS (n = 173).